Geophysical Journal International

*Geophys. J. Int.* (2010) **182,** 1493–1508 doi: 10.1111/j.1365-246X.2010.04690.x

# Determination of the material damping ratio in the soil from SASW tests using the half-power bandwidth method

S. A. Badsar,[1] M. Schevenels,[1] W. Haegeman[1,2,3] and G. Degrande[1]

[1] *Department of Civil Engineering, K.U. Leuven, Kasteelpark Arenberg* 40, B-3001 *Leuven, Belgium. E-mail: mattias.schevenels@bwk.kuleuven.be*
[2] *Department of Industrial Engineering Sciences, KHBO, Zeedijk* 101, B-8400 *Ostend, Belgium*
[3] *Department of Civil Engineering, Ghent University, Technologiepark* 905, B-9052 *Zwijnaarde, Belgium*

Accepted 2010 June 3. Received 2010 June 2; in original form 2009 July 30

## SUMMARY

This paper presents a novel technique for the determination of the material damping ratio in shallow soil layers. It is based on the spectral analysis of surface waves (SASW) test. The technique is an alternative to existing methods, where the damping ratio is determined from the spatial decay of the Rayleigh wave. These methods rely on the knowledge of the geometric damping, and may lead to incorrect results if the geometric damping is calculated based on an inaccurate shear wave velocity profile. The existing methods may also lead to incorrect results when higher modes contribute to the wavefield in the soil.

In the proposed technique, the wavefield is transformed to the frequency–wavenumber domain. The resulting frequency–wavenumber spectrum exhibits a peak that corresponds to the fundamental Rayleigh wave. The dispersion curve is derived from the peak's position, whereas the attenuation curve is derived from its width, using the half-power bandwidth method. Due to the use of the appropriate wavenumber transformation, this method does not require the calculation of the geometric damping. In addition, the occurrence of higher Rayleigh modes does not affect the attenuation curve associated with the fundamental Rayleigh wave, as higher modes appear as separate peaks in the frequency–wavenumber spectrum that do not interfere with the peak corresponding to the fundamental Rayleigh wave (except at the osculation points).

Three benchmark problems are considered to validate the outlined technique; the results are compared with those obtained using existing methods. All methods perform well when applied to a regular soil profile, where the stiffness of the soil increases with depth. For soil profiles with a soft layer trapped between two stiffer layers, or where the soil properties vary smoothly with depth, the proposed technique yields more accurate results than the existing methods.

The practical applicability of the new method is finally illustrated using experimental data collected from a test site in Belgium.

**Key words:** Fourier analysis; Inverse theory; Surface waves and free oscillations; Seismic attenuation; Wave propagation.



## 1 INTRODUCTION

The spectral analysis of surface waves (SASW) method aims to determine the dynamic shear modulus and the material damping ratio of shallow soil layers (Nazarian *et al.* 1983). It is based on an *in situ* experiment where Rayleigh waves are generated by means of an impact hammer, a falling weight or a hydraulic shaker. The resulting wavefield is recorded by a number $M$ of sensors at the soil's surface. The dispersion and attenuation curves of the soil are subsequently determined from the transfer function between the point force and the free field response. An inverse problem is finally solved to identify the corresponding soil profile.

Alternative techniques to determine dynamic soil properties include both laboratory methods and *in situ* methods. Laboratory measurements such as the resonant column test or the torsional shear test are often used to determine properties of cohesive soils, but for non-cohesive soils, there is a risk of sample disturbance. Although laboratory tests are useful for parametric studies of soil properties (Rix *et al.* 2000), *in situ* tests preserve the natural status of the soil and avoid sample disturbance. Moreover, a larger volume of the soil is examined in an *in situ* test, avoiding a bias in the results due to local variations of the soil properties. Among the most accurate *in situ* tests are the borehole methods (i.e. the up-hole, down-hole, and cross-hole test). These techniques have a

good resolution compared to surface wave methods, especially at large depths. However, they are expensive due to the need for one or more boreholes.

The SASW method has been used in different applications over the past couple of decades: to investigate pavement systems (Nazarian & Stokoe 1984), to assess the quality of ground improvement (Cuellar & Valerio 1997), to determine the thickness of waste deposits (Kavazanjian *et al.* 1994) and to identify the dynamic soil properties for the prediction of ground vibrations (Pyl *et al.* 2004; Lombaert *et al.* 2006; Masoumi *et al.* 2007). The most important soil properties in the prediction of ground vibrations are the dynamic shear modulus and the material damping ratio.

Although the SASW method is a well-established technique for the determination of the soil's dynamic shear modulus (Nazarian & Stokoe 1984; Nazarian & Desai 1993; Al-Hunaidi 1994; Gucunski 1994), the application to the determination of the material damping ratio has only recently been tackled (Lai 1998; Rix *et al.* 2000; Foti 2004). Existing methods are all based on the measurement of the spatial decay of surface waves. The spatial decay is due to both the dissipation of energy (material damping) and the spreading of the wave fronts over an increasing area (geometric damping). Geometric damping is accounted for through the use of a geometric spreading factor, which is calculated based on the shear wave velocity profile of the soil. Lai (1998) and Lai *et al.* (2002) developed a technique based on phase and amplitude regression to simultaneously determine the shear wave velocity and material damping ratio of soils. The method involves an iterative update of the geometric spreading factor. For a weakly damped material, Rix *et al.* (2000) simplified the technique by uncoupling the determination of the shear wave velocity and material damping ratio. Foti (2004) used a formulation based on the deconvolution of seismic traces to extend the technique proposed by Rix *et al.* (2000) to SASW tests where the source wavelet is not known.

Forbriger (2003b) developed a waveform fitting method based on a joint inversion of the frequency–wavenumber content of the wavefield in the soil and the *P*-wave arrival time to infer the subsurface properties. The technique is conceptually simple and theoretically appropriate for the determination of the material damping ratio, but the inversion scheme requires a lot of manual interventions to avoid convergence to a local minimum. Guzina & Madyarov (2005) showed that the use of Love waves is a sound alternative to Rayleigh waves as it reduces the number of material parameters relevant to site characterization by precluding the effect of Poisson's ratio and the material damping ratio for dilatational waves. In this approach, the wave motion in the layered half-space is induced by means of a torsionally vibrating disk at the soil's surface, which is difficult to realize in practice.

The surface wave methods established by Lai (1998), Lai *et al.* (2002), Rix *et al.* (2000) and Foti (2004) to determine the material damping ratio are based on the hypothesis that the response of the soil in the SASW test is due to a single-surface mode. If multiple surface modes contribute to the response (e.g. due to a high stiffness contrast or the inclusion of a softer layer), this assumption does not hold and the resulting attenuation curves are incorrect. Moreover, the estimate of the attenuation curve is based on an estimate of the geometric spreading factor. The latter is computed using the shear wave velocity of the soil, which is determined by inversion of the experimental dispersion curve. Inaccuracies in the experimental dispersion curve or the inversion procedure (e.g. due to the non-uniqueness of the inverse problem) may lead to an incorrect estimate of the geometric spreading factor and, consequently, an incorrect experimental attenuation curve.

In this paper, a novel method for the determination of the material damping ratio is proposed, based on the half-power bandwidth method. This method has originally been developed in the field of mechanical and structural dynamics to determine the modal damping ratio of a structure from the width of the peaks in the structure's frequency response function. In this paper, the half-power bandwidth method is applied to the wavenumber content of the soil's response. The occurrence of multiple Rayleigh modes does not affect the resulting attenuation curve of the fundamental Rayleigh wave, as all modes appear as separate, non-interfering peaks in the frequency–wavenumber spectrum (except at the osculation points). Moreover, due to the use of the appropriate wavenumber transformation, this method does not require the calculation of a geometric spreading factor.

The new method is compared with two existing methods where the attenuation curve is determined from the soil's response in the frequency–space domain: a method proposed by Lai *et al.* (2002), where the dispersion and attenuation curves are determined simultaneously, and a method presented by Rix *et al.* (2000), where they are determined independently. These methods are referred to as methods 1 and 2, respectively, whereas the new method is referred to as method 3. The three methods are explained in detail in Section 2.

Three synthetic soil profiles are used as benchmark problems for both the existing methods and the half-power bandwidth method: (1) a soft layer on a stiffer half-space, (2) a soil profile with inverse layering and (3) a soil profile where the properties vary smoothly with depth. The results are discussed in Section 3.

Finally, a real example is considered in Section 4, where the three methods are used to determine the material damping ratio in the soil at a test site in Belgium.

## 2 METHODOLOGY

This section addresses three methods to determine the dispersion and attenuation curves of a layered soil from an SASW experiment. Two existing methods are described in Sections 2.1 and 2.2. The new technique based on the half-power bandwidth method is introduced in Section 2.3.

### 2.1 Phase and amplitude regression in the frequency–space domain

This subsection focuses on the method developed by Lai *et al.* (2002), which is referred to as method 1. Method 1 proceeds as follows.

An SASW experiment is first performed. Rayleigh waves are generated by means of a point force, using an impact hammer, a falling weight or a hydraulic shaker. The resulting wavefield is recorded by a number of sensors along a straight measurement line at the soil's surface. The point force is denoted as $F_z^{\mathrm{E}}(t)$ and the vertical displacement as $u_z^{\mathrm{E}}(r, t)$, where $t$ is the time and $r$ the source–receiver distance. The location of the $j$th receiver is denoted as $r_j$.

The frequency content $\hat{F}_z^{\mathrm{E}}(\omega)$ of the force $F_z^{\mathrm{E}}(t)$ is computed by means of a forward Fourier transformation from the time $t$ to the circular frequency $\omega$:

$$\hat{F}_z^{\mathrm{E}}(\omega) = \int_{-\infty}^{\infty} F_z^{\mathrm{E}}(t) \mathrm{e}^{-i\omega t}\, \mathrm{d}t. \tag{1}$$

The frequency content $\hat{u}_z^{\mathrm{E}}(r,\omega)$ of the displacement $u_z^{\mathrm{E}}(r,t)$ is computed in a similar way:

$$\hat{u}_z^{\mathrm{E}}(r,\omega) = \int_{-\infty}^{\infty} u_z^{\mathrm{E}}(r,t)\mathrm{e}^{-i\omega t}\,\mathrm{d}t. \tag{2}$$

The transfer function $\hat{H}_{zz}^{\mathrm{E}}(r,\omega)$ from the force $\hat{F}_z^{\mathrm{E}}(\omega)$ to the displacement $\hat{u}_z^{\mathrm{E}}(r,\omega)$ is defined as

$$\hat{H}_{zz}^{\mathrm{E}}(r,\omega) = \frac{\hat{u}_z^{\mathrm{E}}(r,\omega)}{\hat{F}_z^{\mathrm{E}}(\omega)}. \tag{3}$$

To improve the signal-to-noise ratio, this transfer function is usually computed by averaging the results obtained for a large number of measurements, using the $H_1$ estimator (Ewins 1984).

The experimental dispersion curve $C_{\mathrm{R}}^{\mathrm{E}}(\omega)$ and attenuation curve $A_{\mathrm{R}}^{\mathrm{E}}(\omega)$ are subsequently determined by means of a phase and amplitude regression scheme, using the transfer function $\hat{H}_{zz}^{\mathrm{E}}(r,\omega)$. This approach is based on the assumption that the response of the soil due to a vertical harmonic point load at the surface only consists of a single surface wave and can be expressed as a product $\hat{h}_{zz}^{\mathrm{E}}(r,\omega)$ of three factors:

$$\hat{h}_{zz}^{\mathrm{E}}(r,\omega) = \zeta(r,\omega)\exp\left(-i\frac{\omega}{C_{\mathrm{R}}^{\mathrm{E}}(\omega)}r\right)\exp\left(-A_{\mathrm{R}}^{\mathrm{E}}(\omega)r\right). \tag{4}$$

The factor $\zeta(r,\omega)$ accounts for the wave decay due to the geometric spreading of the wave fronts over an increasing area. This factor is equal to the displacement amplitude in a soil without material damping and depends on the stratification of the soil. As the stratification is initially unknown, the geometric spreading factor is initially assumed to be equal to the factor in a homogeneous half-space, that is $\zeta(r,\omega) = 1/\sqrt{r}$. The second factor $\exp(-i\omega r/C_{\mathrm{R}}^{\mathrm{E}}(\omega))$ in eq. (4) is a harmonic function that depends on the phase velocity $C_{\mathrm{R}}^{\mathrm{E}}(\omega)$ of the surface wave. The third factor $\exp(-A_{\mathrm{R}}^{\mathrm{E}}(\omega)r)$ is an exponentially decaying function that accounts for the wave decay due to material damping. The decay rate or attenuation coefficient is denoted as $A_{\mathrm{R}}^{\mathrm{E}}(\omega)$.

For each frequency, the phase velocity $C_{\mathrm{R}}^{\mathrm{E}}(\omega)$ and the attenuation coefficient $A_{\mathrm{R}}^{\mathrm{E}}(\omega)$ are determined by fitting the function $\hat{h}_{zz}^{\mathrm{E}}(r,\omega)$ to the experimental transfer function $\hat{H}_{zz}^{\mathrm{E}}(r,\omega)$. In this paper, the fitting procedure is performed in three steps.

The first step involves an amplitude regression analysis: the moduli of the functions $\hat{h}_{zz}^{\mathrm{E}}(r,\omega)$ and $\hat{H}_{zz}^{\mathrm{E}}(r,\omega)$ are fitted at the receiver locations $r_j$ to determine the attenuation coefficient $A_{\mathrm{R}}^{\mathrm{E}}(\omega)$:

$$A_{\mathrm{R}}^{\mathrm{E}}(\omega) = \arg\min_{A}\sum_{j=1}^{M}\left|\left|\hat{H}_{zz}^{\mathrm{E}}(r_j,\omega)\right| - \left|\zeta(r_j,\omega)\exp(-Ar_j)\right|\right|^2. \tag{5}$$

This minimization problem is solved by means of the simplex method proposed by Nelder & Mead (1965).

The second step is a phase regression analysis: the attenuation coefficient $A_{\mathrm{R}}^{\mathrm{E}}(\omega)$ is kept fixed and the complex valued functions $\hat{h}_{zz}^{\mathrm{E}}(r,\omega)$ and $\hat{H}_{zz}^{\mathrm{E}}(r,\omega)$ are fitted at the receiver locations $r_j$ to determine the phase velocity $C_{\mathrm{R}}^{\mathrm{E}}(\omega)$:

$$C_{\mathrm{R}}^{\mathrm{E}}(\omega) = \arg\min_{C}\sum_{j=1}^{M}\left|\hat{H}_{zz}^{\mathrm{E}}(r_j,\omega) - \zeta(r_j,\omega) \times \exp\left(-i\frac{\omega}{C}r_j\right)\exp\left(-A_{\mathrm{R}}^{\mathrm{E}}(\omega)r_j\right)\right|^2. \tag{6}$$

The objective function of this minimization problem exhibits a large number of local minima. To determine the global minimum, the objective function is evaluated for a large number of equally spaced phase velocities $C$ within an interval that is sufficiently wide to contain the actual Rayleigh wave velocity $C_{\mathrm{R}}^{\mathrm{E}}(\omega)$.

These two preliminary analyses provide a starting point for the actual phase and amplitude regression, which is similar to the analysis performed in the previous step but where both the phase velocity $C_{\mathrm{R}}^{\mathrm{E}}(\omega)$ and the attenuation coefficient $A_{\mathrm{R}}^{\mathrm{E}}(\omega)$ are allowed to vary:

$$\left\{C_{\mathrm{R}}^{\mathrm{E}}(\omega),\, A_{\mathrm{R}}^{\mathrm{E}}(\omega)\right\} = \arg\min_{\{C,A\}}\sum_{j=1}^{M}\left|\hat{H}_{zz}^{\mathrm{E}}(r_j,\omega) - \zeta(r_j,\omega)\exp\left(-i\frac{\omega}{C}r_j\right)\exp(-Ar_j)\right|^2. \tag{7}$$

The objective function in this equation also shows a lot of local minima, but the use of a well-chosen starting point justifies the application of a local optimization scheme to find the global minimum. The Nelder–Mead simplex method is used.

Next, an inverse problem is solved to determine the shear wave velocity profile corresponding to the experimental dispersion curve $C_{\mathrm{R}}^{\mathrm{E}}(\omega)$. This profile is used to compute a new estimate of the geometric spreading factor $\zeta(r,\omega)$ and the procedure is repeated until convergence is reached. An additional inverse problem is eventually solved to determine the material damping ratio of the soil corresponding to the experimental attenuation curve $A_{\mathrm{R}}^{\mathrm{E}}(\omega)$.

### 2.2 Frequency–wavenumber analysis and amplitude regression

This subsection addresses the method proposed by Rix *et al.* (2000), which is referred to as method 2. The dispersion curve is first determined from the frequency–wavenumber content of the soil's response in the SASW test. The attenuation curve is subsequently obtained in a similar way as in method 1, according to eq. (5).

The experimental transfer function $\hat{H}_{zz}^{\mathrm{E}}(r,\omega)$ defined in the previous subsection is transformed to the frequency–wavenumber domain (Forbriger 2003a). Several procedures have been presented in the literature to perform this transformation. Among the most popular is the slant stack analysis (McMechan & Yedlin 1981), which is based on a discrete approximation of a Fourier transformation from the spatial coordinate $r$ to the wavenumber $k_r$. In this paper, the procedure proposed by Forbriger (2003a) is followed. This procedure is similar to a classical slant stack analysis, but the Fourier transformation is replaced by a Hankel transformation. In this way, the cylindrical symmetry of the wavefield is properly accounted for, and a decomposition of the wavefield in plane waves is obtained. The frequency–wavenumber spectrum of the response is thus computed as

$$\tilde{H}_{zz}^{\mathrm{E}}(k_r,\omega) = \int_0^{\infty}\hat{H}_{zz}^{\mathrm{E}}(r,\omega)J_0(k_r r)r\,\mathrm{d}r, \tag{8}$$

where $k_r$ is the radial wavenumber and $J_0(k_r r)$ is the zeroth-order Bessel function of the first kind. Eq. (8) is approximated by truncation of the integral at $r = r_{\max}$ (the array length, i.e. the position of the farthest receiver). Following Forbriger (2003a), the Bessel function $J_0(k_r r)$ in eq. (8) is replaced by the zeroth-order Hankel function $H_0^{(1)}(k_r r)/2$ of the first kind to account for the fact that the wavefield only consists of outgoing waves. The following approximation is thus obtained:

$$\tilde{H}_{zz}^{\mathrm{E}}(k_r,\omega) = \frac{1}{2}\int_0^{r_{\max}}\hat{H}_{zz}^{\mathrm{E}}(r,\omega)H_0^{(1)}(k_r r)r\,\mathrm{d}r. \tag{9}$$

The surface waves occur as peaks in the resulting frequency–wavenumber spectrum $\tilde{H}^{\mathrm{E}}_{zz}(k_r, \omega)$. The dispersion curve of the fundamental Rayleigh wave is determined from the position of the first peak in the frequency–wavenumber spectrum. Next, an inverse problem is solved to determine the shear wave velocity profile corresponding to the experimental dispersion curve $C^{\mathrm{E}}_{\mathrm{R}}(\omega)$. This profile is used to compute the geometric spreading factor $\zeta(r, \omega)$. The moduli of the functions $\hat{h}^{\mathrm{E}}_{zz}(r, \omega)$ and $\hat{H}^{\mathrm{E}}_{zz}(r, \omega)$ are subsequently fitted in a similar way as in the first method to determine the attenuation curve $A^{\mathrm{E}}_{\mathrm{R}}(\omega)$. No iteration is required in this method because the geometric spreading factor $\zeta(r, \omega)$ is calculated in a direct way and does not need to be updated. Finally, a second inverse problem is solved to determine the material damping ratio of the soil corresponding to the experimental attenuation curve $A^{\mathrm{E}}_{\mathrm{R}}(\omega)$.

### 2.3 Frequency–wavenumber analysis combined with the half-power bandwidth method

A novel method to determine the attenuation curve is presented. This method is based on the width of the peaks in the frequency–wavenumber spectrum $\tilde{H}^{\mathrm{E}}_{zz}(k_r, \omega)$. First, the peak corresponding to the fundamental surface wave (the first peak) is identified. The dispersion curve is derived from the peak's position in the same way as in the second method discussed in the previous subsection. The attenuation coefficient $A^{\mathrm{E}}_{\mathrm{R}}(\omega)$ is derived from the peak's width: if the attenuation is weak, the peak is high and narrow; if the attenuation is strong, the peak is low and wide. To this end, the half-power bandwidth method is used.

The half-power bandwidth method has originally been developed in the field of mechanical and structural dynamics to determine the modal damping ratio $\xi$ of a structure from the width of the peaks in its frequency response function. The half-power bandwidth $\Delta\omega$ is defined as the width of the peak where the magnitude of the frequency response function is $1/\sqrt{2}$ times the peak value (Chopra 2007). For a weakly damped single degree of freedom system, the damping ratio $\xi$ is then obtained as follows:

$$\xi = \frac{\Delta\omega}{2\omega_{\mathrm{res}}}, \tag{10}$$

where $\omega_{\mathrm{res}}$ is the resonance frequency. The impulse response of the system is a harmonic function that decays exponentially with time. The temporal decay rate $A = \omega_{\mathrm{res}}\xi$ is equal to

$$A = \frac{\Delta\omega}{2}. \tag{11}$$

The half-power bandwidth method is also applicable to the eigenmodes of a multidegree of freedom system with widely spaced resonance frequencies. To avoid mixing of adjacent peaks in the frequency response function, a more general form of the method can be used where the bandwidth $\Delta\omega$ is defined as the width of the peak where the magnitude of the frequency response function is $\gamma$ times the peak value, with $\gamma$ smaller than but close to 1. The damping ratio $\xi$ is then given by

$$\xi = \frac{\Delta\omega}{2\omega_{\mathrm{res}}\sqrt{\gamma^{-2} - 1}}. \tag{12}$$

For $\gamma = 1/\sqrt{2}$, this equation reduces to eq. (10). The temporal decay rate $A = \omega_{\mathrm{res}}\xi$ of the modal impulse response function is obtained as

$$A = \frac{\Delta\omega}{2\sqrt{\gamma^{-2} - 1}}. \tag{13}$$

In this paper, the half-power bandwidth method is applied to the representation of the response of a semi-infinite soil in the frequency–wavenumber domain. The frequency–wavenumber spectrum $\tilde{H}^{\mathrm{E}}_{zz}(k_r, \omega)$ is computed in a similar way as in the previous subsection. However, the truncation of the integral in eq. (8) at $r = r_{\max}$ may result in a widening of the Rayleigh peak in the frequency–wavenumber spectrum, and consequently an overestimation of the attenuation coefficient. To mitigate this effect, a window $\hat{w}(r, \omega)$ that decays exponentially with the distance $r$ is applied to the data in the frequency–space domain. A similar windowing technique is commonly used in mechanical and structural dynamics to determine the damping ratio of weakly damped systems from a free vibration signal with a limited length in time (Fladung & Rost 1997). The application of an exponential window can be considered as the introduction of artificial damping, resulting in a stronger spatial decay of the surface waves. The window $\hat{w}(r, \omega)$ is defined as follows:

$$\hat{w}(r, \omega) = \mathrm{e}^{-\hat{A}_{\mathrm{art}}(\omega)r}. \tag{14}$$

The decay rate is determined by the exponent $\hat{A}_{\mathrm{art}}(\omega)$. For each frequency, the exponent $\hat{A}_{\mathrm{art}}(\omega)$ is chosen as the smallest nonnegative value that satisfies the following inequality:

$$\frac{\left|\hat{w}(r_{\max}, \omega)\hat{H}^{\mathrm{E}}_{zz}(r_{\max}, \omega)\right|}{\left|\hat{w}(r_{\min}, \omega)\hat{H}^{\mathrm{E}}_{zz}(r_{\min}, \omega)\right|} \leq q, \tag{15}$$

where $r_{\min}$ and $r_{\max}$ denote the positions of the nearest and the farthest receiver, respectively. The application of the window ensures that the amplitude ratio of the response at the farthest and the nearest receiver does not exceed a value $q$. The choice of the value $q$ is addressed in Section 3.1, where the half-power bandwidth method is applied to the first benchmark problem.

At every frequency $\omega$, the peak corresponding to the fundamental Rayleigh wave is identified. The bandwidth $\Delta k_r(\omega)$ is determined as the width of the peak where the magnitude of the transfer function $\tilde{H}^{\mathrm{E}}_{zz}(k_r, \omega)$ reaches $\gamma$ times the peak value. The corresponding spatial decay rate or attenuation coefficient $A^{\mathrm{E}}_{\mathrm{R}}(\omega)$ is given by

$$A^{\mathrm{E}}_{\mathrm{R}}(\omega) = \frac{\Delta k_r(\omega)}{2\sqrt{\gamma^{-2} - 1}}. \tag{16}$$

The value obtained is affected by the exponential window $\hat{w}(r, \omega)$ defined in eq. (14). The true value of the attenuation coefficient $A^{\mathrm{E}}_{\mathrm{R}}(\omega)$ is retrieved by subtracting the artificial attenuation coefficient $\hat{A}_{\mathrm{art}}(\omega)$.

In this alternative approach, the occurrence of multiple Rayleigh modes has no impact on the attenuation curve of the fundamental Rayleigh wave, as all modes occur as separate peaks in the frequency–wavenumber spectrum $\tilde{H}^{\mathrm{E}}_{zz}(k_r, \omega)$ (except at the osculation points). Moreover, the identified attenuation curve is derived directly from the experimental data, avoiding the use of a (possibly incorrect) estimate of the soil's shear wave velocity.

## 3 BENCHMARK PROBLEMS

In this section, both the existing methods and the new method to determine the dispersion and attenuation curves of a layered soil are applied to three synthetic soil profiles: a regular soil profile consisting of a soft layer on a stiffer half-space, an irregular soil profile where a soft layer is trapped between two stiffer layers and a soil profile where the properties vary smoothly with depth.

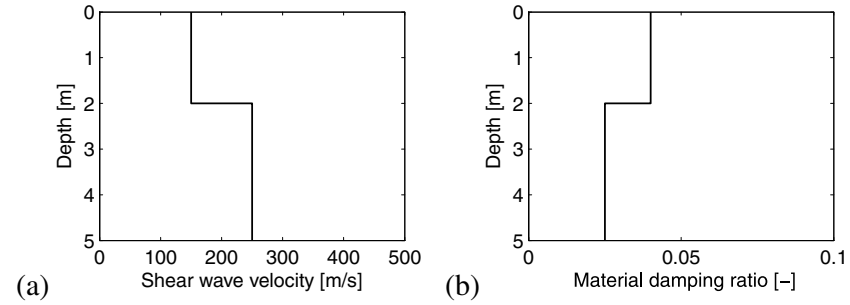


**Figure 1.** (a) Shear wave velocity and (b) material damping ratio for the regular soil profile.

### 3.1 Regular soil profile

The first soil profile is shown in Fig. 1. It consists of a layer with a thickness of 2 m on a half-space. The shear wave velocity $C_s$ is 150 m s$^{-1}$ in the layer and 250 m s$^{-1}$ in the half-space. Poisson's ratio $\nu$ is 1/3 throughout the medium, resulting in a dilatational wave velocity $C_p$ of 300 m s$^{-1}$ in the layer and 500 m s$^{-1}$ in the half-space. Material damping is modelled through the use of complex Lamé coefficients $\mu^* = \mu(1+2iD_s)$ and $(\lambda+2\mu)^* = (\lambda+2\mu)(1+2iD_p)$, where $D_s$ and $D_p$ represent the hysteretic material damping ratios for shear and dilatational waves, respectively. An identical value $D = D_s = D_p$ for both types of waves is used, equal to 0.04 in the layer and 0.025 in the half-space. The density $\rho$ is 1900 kg m$^{-3}$ everywhere.

An SASW experiment is simulated as follows. The response of the soil due to a vertical point load at the surface is first determined. In reality, the point load is generated by means of an impact hammer, a falling weight, or a hydraulic shaker. In the simulation, a transient point load is considered, and the loading function $F_z^E(t)$ is a Ricker wavelet:

$$F_z^E(t) = \left[2\left(\frac{\pi(t-t_s)}{T_D}\right)^2 - 1\right]\exp\left[-\left(\frac{\pi(t-t_s)}{T_D}\right)^2\right], \qquad (17)$$

where $t_s = 0.05$ s is a time shift and $T_D = 0.03$ s is the characteristic period. This period is chosen in an attempt to simulate the frequency content of a hammer impact in an actual SASW test. The time history $F_z^E(t)$ and the frequency content $\hat{F}_z^E(\omega)$ of the loading function are shown in Fig. 2.

The resulting vertical displacement at the soil's surface $u_z^E(r,t)$ is calculated for an array of 100 equidistant receivers located from 1 to 100 m from the source. The computation is performed by means of the ElastoDynamics Toolbox (EDT) for MATLAB (Schevenels *et al.* 2009), which is based on the direct stiffness method (Kausel & Roësset 1981; Kausel 2006). The results are shown in Fig. 3(a).

The transfer function $\hat{H}_{zz}^E(r,\omega)$ is calculated according to eq. (3) and shown in Fig. 3(b). Due to geometric and material damping in the soil, the transfer function $\hat{H}_{zz}^E(r,\omega)$ decays with the distance $r$. The effect of material damping is frequency dependent, leading to a stronger decay in the higher frequency range.

The transfer function $\hat{H}_{zz}^E(r,\omega)$ is transformed to the frequency–wavenumber domain according to eq. (9). An exponential window $\hat{w}(r,\omega)$ is used. The window is chosen so that the amplitude ratio of the response at the farthest and the nearest receiver is smaller than $q = 10^{-4}$. The choice of the parameter $q$ is discussed at the end of this section. The integral in eq. (9) is evaluated by means of a generalized Filon quadrature scheme (Frazer & Gettrust 1984).

For visualization purposes, the frequency–wavenumber spectrum $\tilde{H}_{zz}^E(k_r,\omega)$ is normalized as follows:

$$\tilde{H}_{zz}^{E,\mathrm{norm}}(k_r,\omega) = \frac{\tilde{H}_{zz}^E(k_r,\omega)}{\max_{k_r}\left|\tilde{H}_{zz}^E(k_r,\omega)\right|}. \qquad (18)$$

The normalized frequency–wavenumber spectrum $\tilde{H}_{zz}^{E,\mathrm{norm}}(k_r,\omega)$ is shown in Fig. 3(c). The spectrum is plotted in terms of the phase velocity $C_r = \omega/k_r$ instead of the wavenumber $k_r$. The maximum in the frequency–wavenumber spectrum corresponds to the dispersion curve of the soil. Fig. 3(c) clearly shows that the wavefield at the soil's surface is dominated by a single Rayleigh wave.

The three methods described in the previous section are used to determine the experimental dispersion curve $C_R^E(\omega)$, using either the transfer function $\hat{H}_{zz}^E(r,\omega)$ (method 1) or the frequency–wavenumber spectrum $\tilde{H}_{zz}^E(k_r,\omega)$ (methods 2 and 3). The resulting curves are shown in Figs 4(1a)–(1c). The curves are confronted with the original dispersion curve, which is directly computed with EDT. The experimental dispersion curve obtained with method 1 differs slightly from the original curve. This is due to the fact that the representation of the wavefield in eq. (4) is not exact. It is based on the assumption that the wavefield is solely due to the Rayleigh wave; the contribution of body waves (which

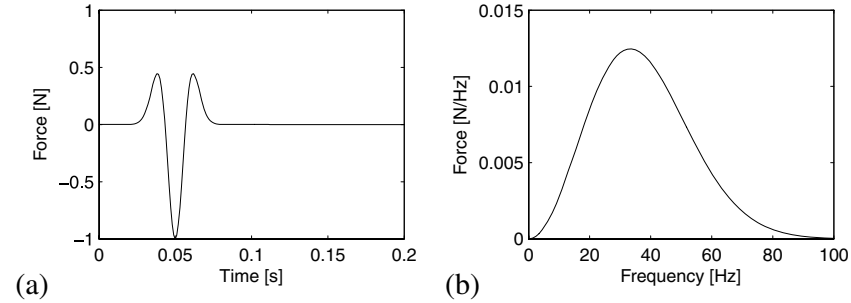


**Figure 2.** (a) Time history $F_z^E(t)$ and (b) frequency content $\hat{F}_z^E(\omega)$ of a Ricker pulse with a characteristic period $T_D = 0.03$ s and a time shift $t_s = 0.05$ s.

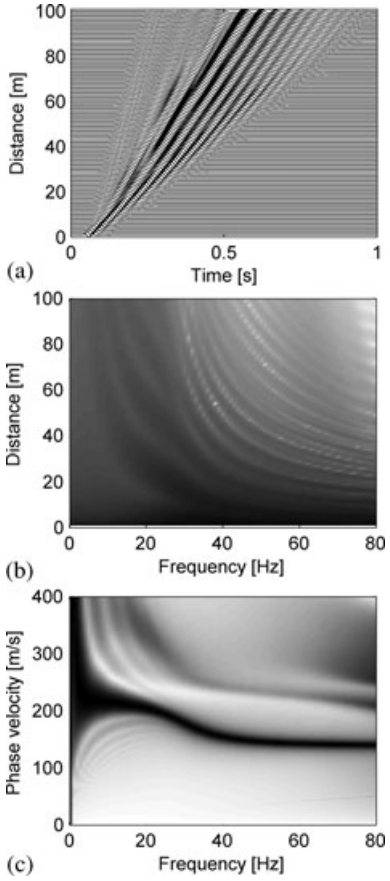


**Figure 3.** (a) Wiggle traces $u_z^{\mathrm{E}}(r, t)$, (b) transfer function $\hat{H}_{zz}^{\mathrm{E}}(r, \omega)$ and (c) frequency–wavenumber spectrum $\tilde{H}_{zz}^{\mathrm{E,norm}}(C_r, \omega)$ for the regular soil profile.

is small but not zero) is not taken into account. The experimental dispersion curve obtained with the other methods shows a very good correspondence with the original curve.

The experimental dispersion curves $C_{\mathrm{R}}^{\mathrm{E}}(\omega)$ obtained with the three methods are used to determine the soil's shear wave velocity $C_{\mathrm{s}}$: an inverse problem is solved where the distance between the experimental and a theoretical dispersion curve is minimized. The theoretical dispersion curve is most sensitive to the shear wave velocity $C_{\mathrm{s}}$ but also shows a slight dependence on the dilatational wave velocity $C_{\mathrm{p}}$. This implies that a value has to be selected for either the dilatational wave velocity $C_{\mathrm{p}}$ or the Poisson's ratio $\nu$. In the present case and in the following synthetic examples, the true value of the Poisson's ratio $\nu = 1/3$ is used in the inversion. The resulting theoretical dispersion curves are shown in Figs 4(1a)–(1c); they perfectly match the experimental curves, indicating a successful inversion. The corresponding shear wave velocity profiles are shown in Figs 4(2a)–(2c). A good agreement with the original profile is observed in the three cases.

The three methods are applied to determine the experimental attenuation curve $A_{\mathrm{R}}^{\mathrm{E}}(\omega)$, using either the transfer function $\hat{H}_{zz}^{\mathrm{E}}(r, \omega)$ (methods 1 and 2), or the frequency–wavenumber spectrum $\tilde{H}_{zz}^{\mathrm{E}}(k_r, \omega)$ (method 3).

Figs 4(3a)–(3c) compare the resulting curves with the original attenuation curve, which is directly computed with EDT. The correspondence is acceptable for the three methods. The oscillations in the experimental attenuation curve obtained with method 1 can be eliminated by reducing the receiver interval in the experimental setup.

The material damping ratio of the soil is determined by solving an inverse problem where the difference between the experimental and a theoretical attenuation curve is minimized. The theoretical curves are shown in Figs 4(3a)–(3c) and correspond well with the experimental curves, revealing a successful inversion. The resulting material damping ratio profiles are shown in Figs 4(4a)–(4c). The correspondence with the original profile is satisfactory for the three methods.

It can be concluded that for a regular soil profile, where the stiffness increases with depth, both the existing methods and the new method to determine the material damping in the soil from an SASW test yield acceptable results.

The half-power bandwidth method requires the choice of the parameter $q$ that determines the strength of the exponential window and the parameter $\gamma$ that determines the amplitude level where the width of the peak in the frequency–wavenumber spectrum is measured. The values used in this example are $q = 10^{-4}$ and $\gamma = 0.99$. These values are chosen based on a parametric study; the results are shown in Fig. 5.

Fig. 5(a) shows the experimental attenuation curve obtained with six different values for the parameter $q$, varying from $10^{-2}$ to $10^{-7}$. The value $q = 10^{-4}$ is selected as the corresponding experimental attenuation curve shows the best agreement with the original curve. The results in the frequency range below 15 Hz are discarded because they are inaccurate for all values of $q$.

Fig. 5(b) shows the experimental attenuation curve obtained with four different values of the parameter $\gamma$, ranging from $1/\sqrt{2}$ to 0.999. For $\gamma = 0.99$ and 0.999, it can be observed that the results have converged (the curves coincide), while still being numerically stable. A value $\gamma = 0.99$ is therefore used.

The same values for the parameters $q$ and $\gamma$ and the threshold frequency of 15 Hz are used in all examples throughout the paper, as the dynamic soil properties are of the same order of magnitude and the experimental setup is identical in all examples, including the real example in Section 4. For cases where the soil profile or the experimental setup is considerably different, it is suggested to repeat the parametric study using adapted soil properties and sensor locations.

### 3.2 Irregular soil profile

The second soil profile is an irregular profile with a soft layer between a stiffer layer and a stiffer half-space. The profile is shown in Fig. 6. The top layer has a thickness of 3 m and the second layer has a thickness of 1 m. The shear wave velocity is equal to 250 m s$^{-1}$ in the top layer, 150 m s$^{-1}$ in the second layer and 400 m s$^{-1}$ in the half-space. Poisson's ratio $\nu$ equals 1/3 throughout the medium, resulting in a dilatational wave velocity of 500 m s$^{-1}$ in the top layer, 300 m s$^{-1}$ in the second layer, and 800 m s$^{-1}$ in the half-space. The material damping ratio $D$ is 0.03 in the top layer, 0.05 in the second layer and 0.01 in the half-space. The density $\rho$ is 1900 kg m$^{-3}$ everywhere.

An SASW experiment is simulated in the same way as for the first synthetic soil profile. The resulting wiggle traces $u_z^{\mathrm{E}}(r, t)$ are shown in Fig. 7, as well as the transfer function $\hat{H}_{zz}^{\mathrm{E}}(r, \omega)$ and the frequency–wavenumber spectrum $\tilde{H}_{zz}^{\mathrm{E,norm}}(C_r, \omega)$. The latter reveals the occurrence of higher modes: multiple maxima can be observed in the frequency–wavenumber spectrum in Fig. 7(c).

The three methods described in Section 2 are used to determine the experimental dispersion curve $C_{\mathrm{R}}^{\mathrm{E}}(\omega)$ and attenuation curve

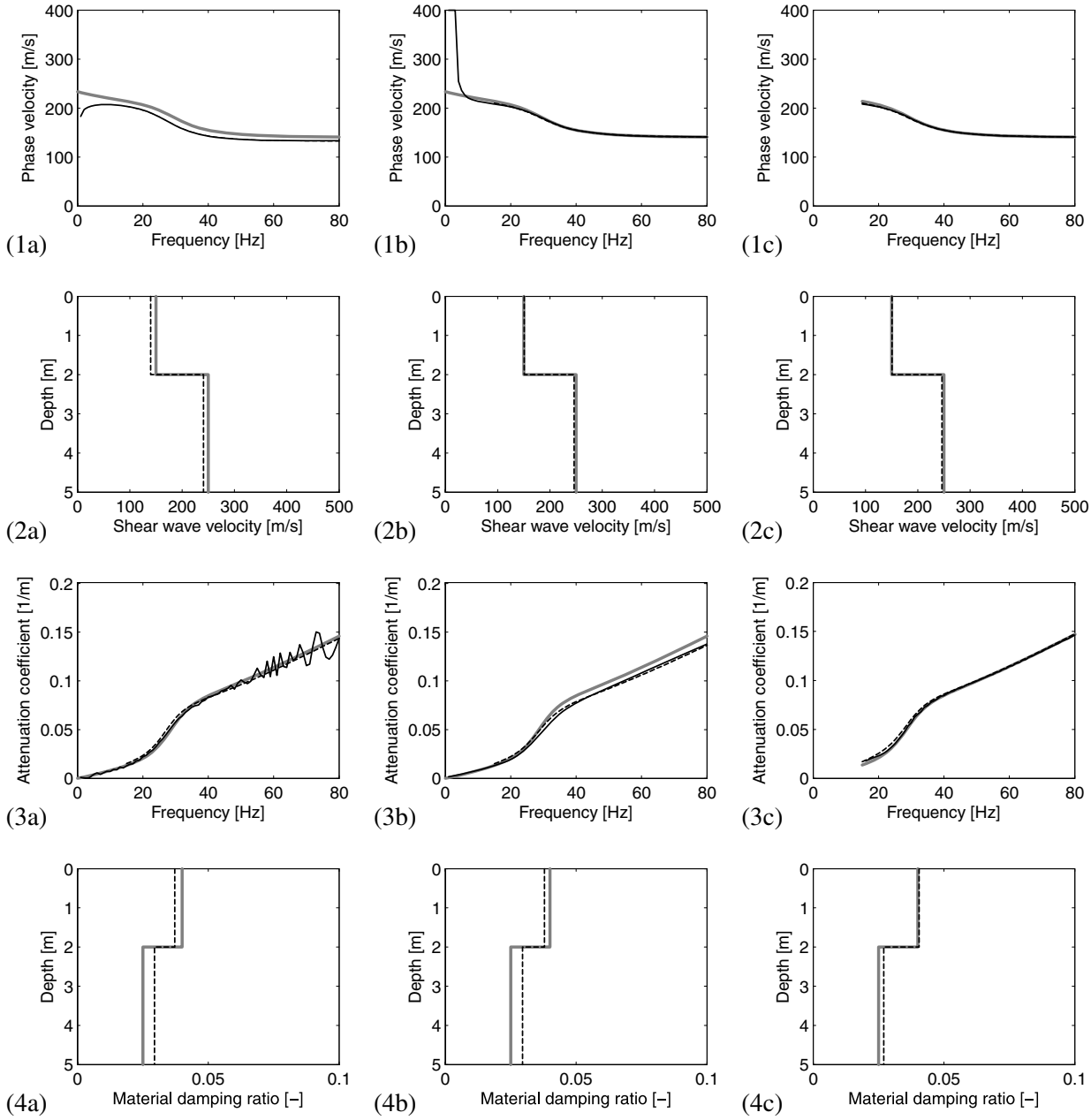


**Figure 4.** (1) Dispersion curve, (2) shear wave velocity, (3) attenuation curve and (4) material damping ratio for the regular soil profile as determined by (a) method 1, (b) method 2 and (c) method 3. The experimental data (solid black lines) and the theoretical data (dashed black lines) are compared with the original data (grey lines).

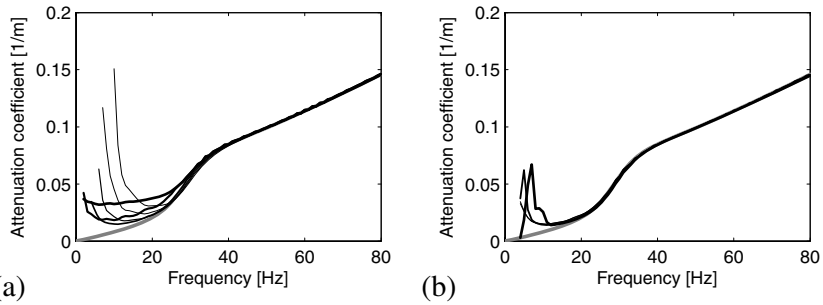


**Figure 5.** Experimental attenuation curve (black lines) for the regular soil profile as determined by method 3, using different values for (a) the parameter $q$ and (b) the parameter $\gamma$. The values used for the parameter $q$ are $10^{-2}$ (thick black line), $10^{-3}, \ldots, 10^{-7}$ (thin black line); the values used for the parameter $\gamma$ are $1/\sqrt{2}$ (thick black line), 0.9, 0.99 and 0.999 (thin black line). The experimental data are compared with the original data (grey lines).

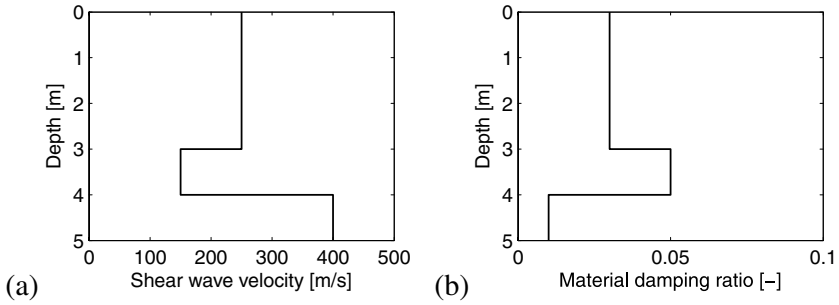


**Figure 6.** (a) Shear wave velocity and (b) material damping ratio for the irregular soil profile.

$A_R^E(\omega)$, as well as the corresponding shear wave velocity $C_s$ and material damping ratio $D$. The results are shown in Fig. 8.

Figs 8(1a)–(1c) show the experimental dispersion curve $C_R^E(\omega)$ as obtained by the three methods. In the three cases, a good correspondence with the original curve is observed.

Figs 8(2a)–(2c) show the shear wave velocity profile identified using the experimental dispersion curves determined by the three methods. The results are in agreement with the original profile.

Figs 8(3a)–(3c) compare the experimental attenuation curve $A_R^E(\omega)$ as obtained by the three different methods with the original attenuation curve. In the case of methods 1 and 2, a misfit is observed in the higher frequency range. This is explained as follows. The response of the soil in the SASW test is assumed to be due to a single surface wave mode. When multiple surface waves contribute to the response, for example due to the inclusion of a softer layer, this assumption is no longer valid, and the resulting attenuation curve is incorrect. Fig. 7(c) shows that higher modes contribute to the response in the frequency range above 60 Hz. Within this range, the experimental attenuation curve consequently deviates from the original attenuation curve, as can be observed in Figs 8(3a) and (3b). The experimental attenuation curve $A_R^E(\omega)$ determined by the new method (method 3), shown in Fig. 8(3c), agrees well with the original curve. This confirms that the contribution of higher modes to the soil's response does not affect the attenuation curve obtained by method 3.

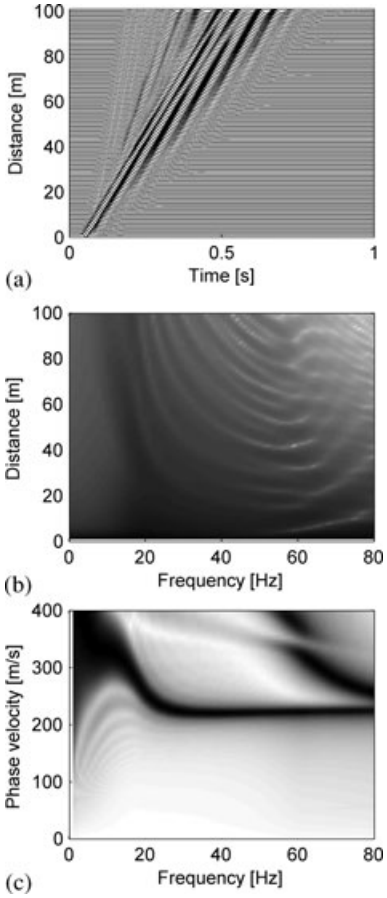


**Figure 7.** (a) Wiggle traces $u_z^E(r, t)$, (b) transfer function $\hat{H}_{zz}^E(r, \omega)$ and (c) frequency–wavenumber spectrum $\tilde{H}_{zz}^{E,norm}(C_r, \omega)$ for the irregular soil profile.

The experimental attenuation curves are inverted to determine the material damping ratio profile. The resulting profiles are shown in Figs 8(4a)–(4c). For method 1, the identified material damping ratio profile does not agree with the original profile, which is obviously due to the use of an erroneous experimental attenuation curve. For method 2, the agreement of the identified material damping ratio profile with the original profile is better, but this is due to a compensation of two errors: (1) the experimental attenuation curve $A_R^E(\omega)$ deviates from the original curve and (2) the inversion procedure has not been successful; it has led to a material damping ratio profile with a theoretical attenuation curve $A_R^T(\omega)$ that does not match the experimental curve $A_R^E(\omega)$. For method 3, a material damping ratio profile matching the original profile is obtained, and the corresponding theoretical attenuation curve $A_R^T(\omega)$ agrees well with the experimental curve $A_R^E(\omega)$.

It can be concluded that the new method performs better than the existing methods in the identification of the material damping in a soil with inverse layering, where higher modes participate in the soil's response.

### 3.3 Smoothly varying soil profile

The third soil profile can be considered as a profile consisting of two layers on a half-space where the material properties vary smoothly between the layers. The profile is shown in Fig. 9. This profile is chosen in an attempt to mimic a real soil where the material properties do not vary abruptly. It is modelled using 33 homogeneous layers with a thickness of 0.1 m on top of a homogeneous half-space. The shear wave velocity $C_s$ increases gradually from 50 m s$^{-1}$ at the surface to 313 m s$^{-1}$ at a depth of 3.3 m. The material damping ratio $D$ decreases with depth, from 0.05 at the surface to 0.025 at a depth of 3.3 m. Poisson's ratio $\nu$ equals 1/3 and the density $\rho$ is equal to 1900 kg m$^{-3}$ throughout the medium.

An SASW experiment is simulated in the same way as for the other synthetic soil profiles. The results are shown in Fig. 10. Fig. 10(c) shows that the soil's response is dominated by a higher mode in the frequency range from 15 to 25 Hz. Outside this range, the fundamental Rayleigh wave is dominant.

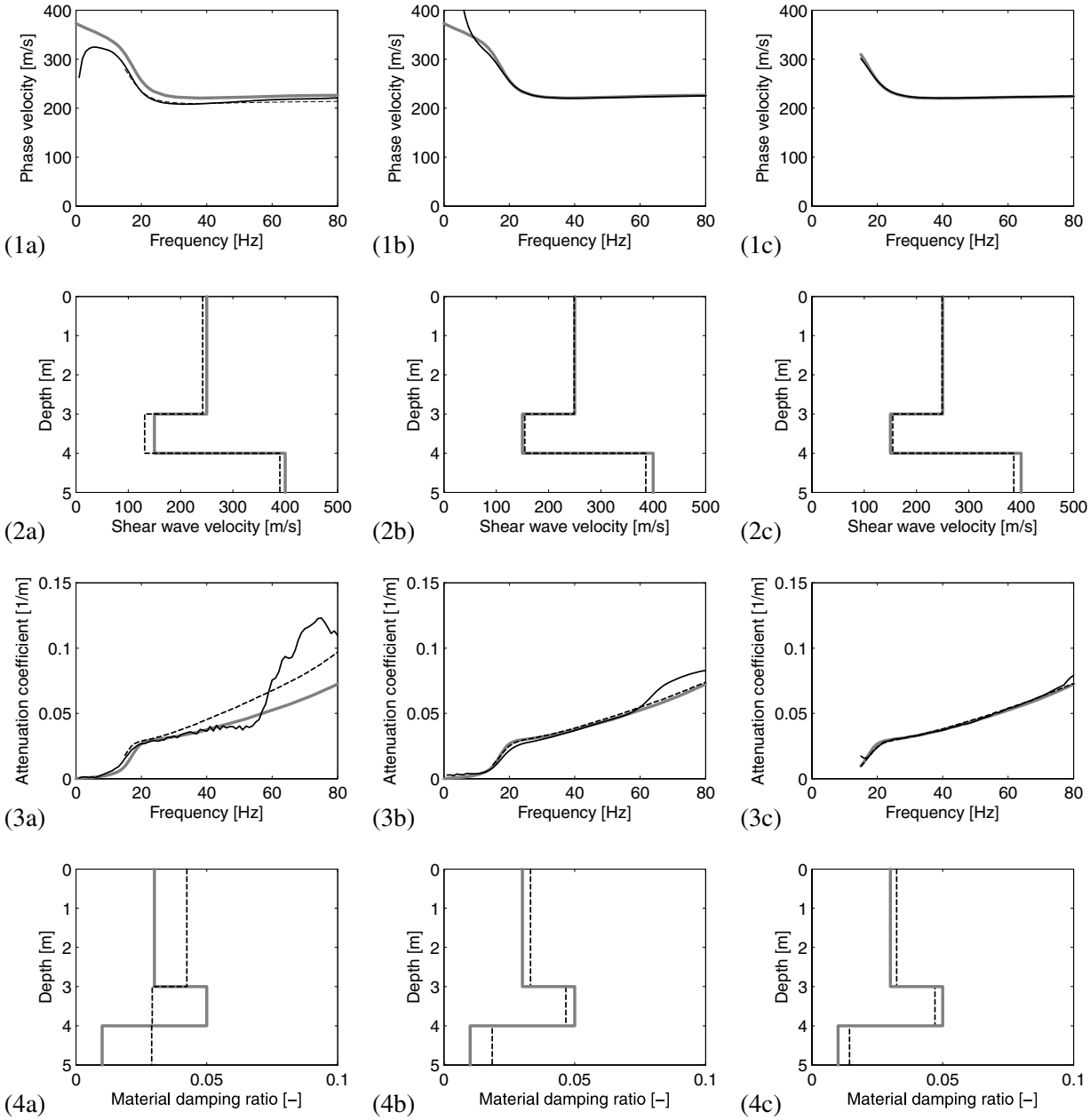


**Figure 8.** (1) Dispersion curve, (2) shear wave velocity, (3) attenuation curve and (4) material damping ratio for the irregular soil profile as determined by (a) method 1, (b) method 2 and (c) method 3. The experimental data (solid black lines) and the theoretical data (dashed black lines) are compared with the original data (grey lines).

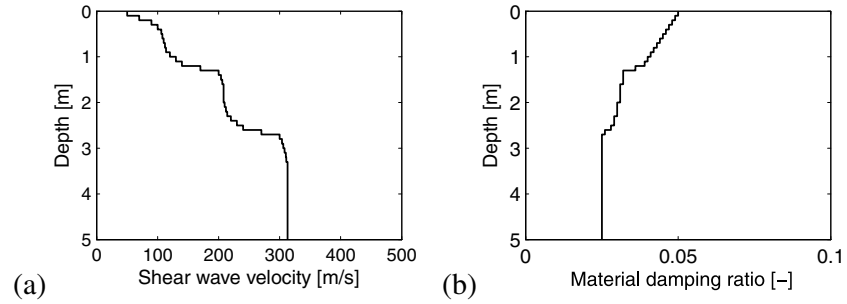


**Figure 9.** (a) Shear wave velocity and (b) material damping ratio for the smoothly varying soil profile.

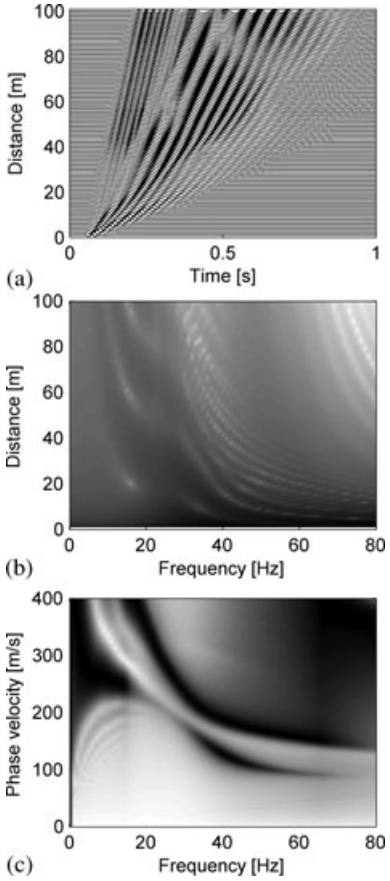


**Figure 10.** (a) Wiggle traces $u_z^{\mathrm{E}}(r, t)$, (b) transfer function $\hat{H}_{zz}^{\mathrm{E}}(r, \omega)$ and (c) frequency–wavenumber spectrum $\tilde{H}_{zz}^{\mathrm{E,norm}}(C_r, \omega)$ for the smoothly varying soil profile.

The three methods described in Section 2 are used to determine the experimental dispersion curve $C_{\mathrm{R}}^{\mathrm{E}}(\omega)$ and attenuation curve $A_{\mathrm{R}}^{\mathrm{E}}(\omega)$. The corresponding shear wave velocity $C_{\mathrm{s}}$ and material damping ratio $D$ are obtained by means of an inversion procedure, where the soil is modelled as a horizontally layered medium. To mimic real practice, the number of layers in the inverse problem is kept as small as possible, but sufficiently large to allow for a good fit between the experimental and the theoretical dispersion and attenuation curves. This approach results in a shear wave velocity profile consisting of two layers on a half-space, and a material damping ratio profile of four layers on a half-space. The results are shown in Fig. 11.

Figs 11(1a)–(1c) compare the experimental dispersion curves $C_{\mathrm{R}}^{\mathrm{E}}(\omega)$ obtained by the three methods with the original curve. The agreement is good in the three cases.

Figs 11(2a)–(2c) show the shear wave velocity profile identified using the experimental dispersion curves determined by the three methods. In the three cases, the resulting two-layers-on-a-half-space profile is an acceptable approximation of the original smoothly varying soil profile.

Figs 11(3a)–(3c) compare the experimental attenuation curve $A_{\mathrm{R}}^{\mathrm{E}}(\omega)$ as obtained by the three different methods with the original attenuation curve. The curves obtained with methods 1 and 2 do not fit the original curve. The misfit cannot be explained by the occurrence of higher modes, as the contribution of these modes to the soil's response is restricted to the frequency range between 15 and 25 Hz, while the misfit arises at higher frequencies. The misfit can be explained by errors in the geometric spreading factor $\zeta(r, \omega)$ in eq. (4). This factor $\zeta(r, \omega)$ is computed using the shear wave velocity profile of the soil, determined by inversion of the experimental dispersion curve. In this case, it is plausible that the geometric spreading factor $\zeta(r, \omega)$ computed using the two-layers-on-a-half-space profile in Fig. 11(2a) or 11(2b) differs from the actual geometric spreading factor $\zeta(r, \omega)$ for the original smoothly varying soil profile, leading to an incorrect estimate of the experimental attenuation curve. In method 3, the geometric spreading factor $\zeta(r, \omega)$ is not used, and the experimental attenuation curve $A_{\mathrm{R}}^{\mathrm{E}}(\omega)$ is derived directly from the experimental data. The resulting curve, shown in Fig. 11(3c), agrees well with the original curve.

Figs 11(4a)–(4c) show the material damping ratio profile as determined from the experimental attenuation curves obtained by the three methods. For methods 1 and 2, the identified material damping ratio profile differs from the original profile, due to the use of an erroneous experimental attenuation curve. For method 3, the agreement is much better.

This synthetic example demonstrates that the new method yields better results than the existing methods in the determination of the material damping in a soil where the properties vary smoothly between the layers, which is likely to occur in reality.

## 4 APPLICATION TO REAL MEASUREMENT DATA

All three methods discussed in Section 2 are applied to data collected at a site in Lincent, Belgium, next to the HST line L2 between Brussels and Liège. In preparation of the construction of the high-speed railway track, borings and cone penetration tests have been carried out at this site. The borings reveal the presence of a silt top layer with a thickness of about 1.2 m, followed by a fine sand layer reaching to a depth of 3.2 m and a sequence of very stiff layers of arenite and clay (Karl 2005; Karl *et al.* 2006). A seismic refraction test has been performed in February 2008 to determine the dilatational wave velocity, resulting in a value of 286 m s$^{-1}$ up to a depth of 4 m and a value of 1667 m s$^{-1}$ at larger depths. The increase of the dilatational wave velocity at a depth of 4 m is probably due to the presence of a ground water table. SCPT tests performed in May 2003 (Karl 2005; Karl *et al.* 2006) have allowed for the determination of the shear wave velocity up to a depth of 6 m: it increases almost linearly from 160 m s$^{-1}$ at 1 m depth to 280 m s$^{-1}$ at 6 m depth. The material damping ratio has also been derived from SCPT tests (Karl *et al.* 2008), resulting in a highly uncertain value between 0.00 and 0.06.

In parallel with the seismic refraction test, an SASW test has been performed in February 2008 (Schevenels *et al.* 2008a). Surface waves have been generated by means of a hammer impact on a 40 cm × 40 cm × 8 cm aluminium foundation. The acceleration at the soil's surface has been measured by means of 100 equidistant receivers, located up to 100 m from the source. Use has been made of PCB 393A03 accelerometers up to 32 m from the source and PCB 393B12, 393A31 and 393B31 accelerometers at larger distances. The data acquisition has been performed with a National Instruments PXI-1050 chassis with four PXI-4472B modules. Fig. 12 shows the acceleration due to a single hammer impact, measured at 10 m, 50 m and 100 m from the source. It is clear that the signal-to-noise ratio in the far field is very low.

To improve the signal-to-noise ratio, 100 hammer impacts have been recorded, and the average displacement transfer function

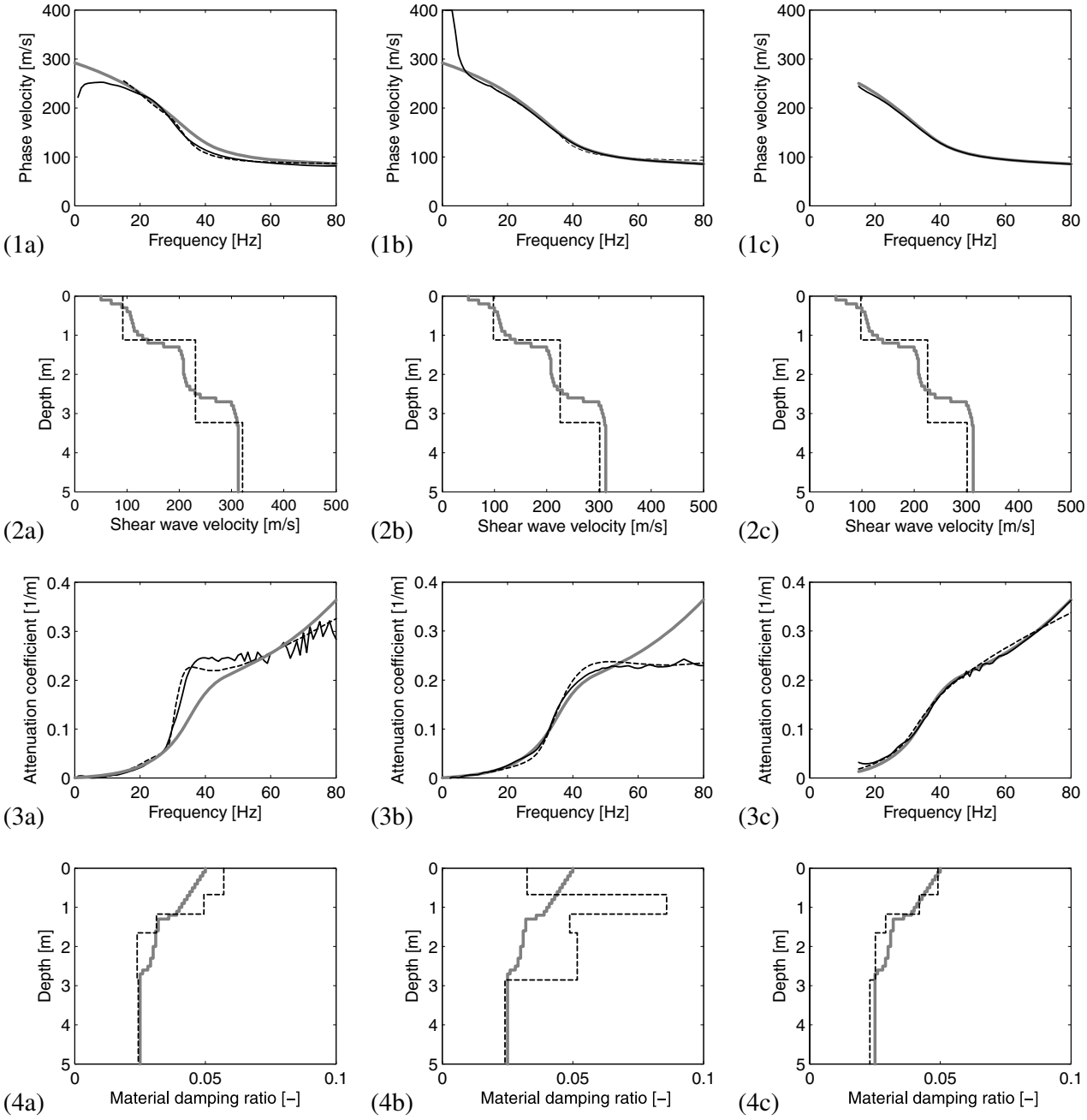


**Figure 11.** (1) Dispersion curve, (2) shear wave velocity, (3) attenuation curve and (4) material damping ratio for the smoothly varying soil profile as determined by (a) method 1, (b) method 2 and (c) method 3. The experimental data (solid black lines) and the theoretical data (dashed black lines) are compared with the original data (grey lines).

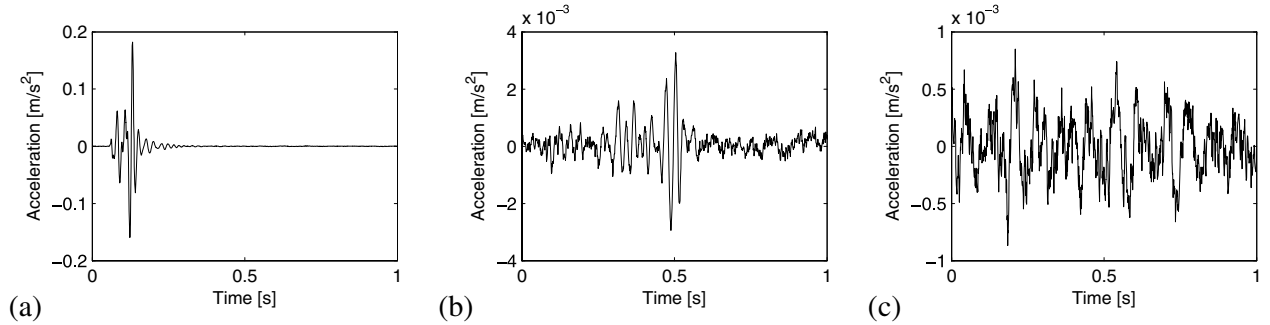


**Figure 12.** Vertical acceleration measured in the SASW test in Lincent at (a) 10 m, (b) 50 m and (c) 100 m from the source.

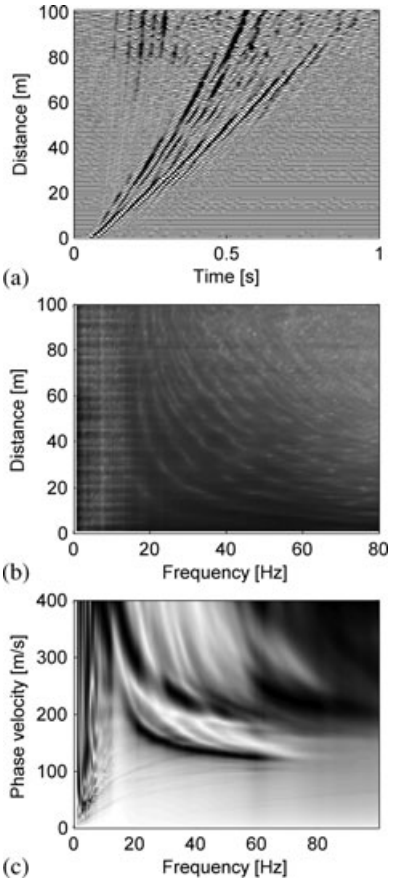


**Figure 13.** (a) Wiggle traces $u_z^{\mathrm{E}}(r, t)$, (b) transfer function $\hat{H}_{zz}^{\mathrm{E}}(r, \omega)$ and (c) frequency–wavenumber spectrum $\tilde{H}_{zz}^{\mathrm{E,norm}}(C_r, \omega)$ for the test site in Lincent.

$\hat{H}_{zz}^{\mathrm{E}}(r, \omega)$ is computed by means of the $H_1$ estimator (Ewins 1984). The transfer function $\hat{H}_{zz}^{\mathrm{E}}(r, \omega)$ is shown in Fig. 13(b).

The transfer function $\hat{H}_{zz}^{\mathrm{E}}(r, \omega)$ is multiplied by a Ricker pulse with a time shift $t_{\mathrm{s}} = 0.05$ s and a characteristic period $T_{\mathrm{D}} = 0.03$ s. An inverse Fourier transformation from the circular frequency $\omega$ to the time $t$ is performed to produce the averaged time signals $u_z^{\mathrm{E}}(r, t)$ shown in Fig. 13(a). These signals $u_z^{\mathrm{E}}(r, t)$ are only computed for the purpose of visualization; they are not used in the further processing. The wiggle traces at adjacent receivers show a good coherence, indicating that the signal-to-noise ratio has improved due to the averaging procedure.

The transfer function $\hat{H}_{zz}^{\mathrm{E}}(r, \omega)$ is transformed to the frequency–wavenumber domain according to eq. (9). An exponential window $\hat{w}(r, \omega)$ is used. The window is chosen so that the amplitude ratio of the response at the farthest and the nearest receiver is smaller than $q = 10^{-4}$. The resulting frequency–wavenumber spectrum $\tilde{H}_{zz}^{\mathrm{E}}(k_r, \omega)$ is shown in Fig. 13(c). Between 15 and 75 Hz, a peak corresponding to the fundamental dispersion curve is clearly visible in this figure. Below 15 Hz, the accuracy of the frequency–wavenumber spectrum $\tilde{H}_{zz}^{\mathrm{E}}(k_r, \omega)$ is too low for a reliable estimation of the dispersion curve $C_{\mathrm{R}}^{\mathrm{E}}(\omega)$. As a consequence, the largest Rayleigh wavelength $\lambda_{\mathrm{Rmax}}^{\mathrm{E}}$ that can be measured is 15 m. Above 75 Hz, the peak corresponding to the first dispersion curve disappears. Theoretically, the highest frequency where the dispersion curve $C_{\mathrm{R}}^{\mathrm{E}}(\omega)$ can be estimated is determined by the distance between two adjacent receivers. The smallest wavelength that can be measured with a distance of 1 m between adjacent receivers equals 2 m. In the high-frequency range (above 75 Hz), the wavelength of the Rayleigh wave is smaller than 2 m. This gives rise to spatial aliasing, resulting in unreliable data that can not be used to determine the dispersion curve $C_{\mathrm{R}}^{\mathrm{E}}(\omega)$.

The experimental dispersion curve $C_{\mathrm{R}}^{\mathrm{E}}(\omega)$ and attenuation curve $A_{\mathrm{R}}^{\mathrm{E}}(\omega)$ as well as the corresponding shear wave velocity $C_{\mathrm{s}}$ and material damping ratio $D$ are determined by means of the three methods discussed in Section 2. Fig. 14 compares the results with the SCPT data.

Figs 14(1a)–(1c) show the experimental dispersion curve $C_{\mathrm{R}}^{\mathrm{E}}(\omega)$ as determined by the three methods. The dispersion curve obtained by method 1 is slightly different from the curve obtained with the other methods, especially in the higher frequency range. The curve obtained with the other methods is probably the most accurate, as method 1 is based on the inexact representation of the wavefield in eq. (4).

The corresponding shear wave velocity profile has been determined up to a relatively small depth of 5 m. This depth is chosen as a function of the largest measured Rayleigh wavelength $\lambda_{\mathrm{Rmax}}^{\mathrm{E}}$. Schevenels *et al.* (2008b) performed a stochastic study to demonstrate that the resolution of the SASW test deteriorates at depths larger than a fraction of the wavelength $\lambda_{\mathrm{Rmax}}^{\mathrm{E}}$. Determining the soil properties at larger depths is possible, but the resolution is much lower, necessitating the use of a regularization technique. In this example, the choice is made to limit the investigation depth and to focus on the region where the resolution of the SASW test is high. In the determination of the shear wave velocity $C_{\mathrm{s}}$, a value for the dilatational wave velocity $C_{\mathrm{s}}$ or the Poisson's ratio $\nu$ has to be selected. In this case, the dilatational wave velocity $C_{\mathrm{b}}$ from the seismic refraction test performed simultaneously with the SASW test is used. The identified shear wave velocity profile is shown in Figs 14(2a)–(2c). It is a regular profile, that is the stiffness increases with depth. The agreement of the profiles obtained by the three methods with the SCPT results is acceptable.

Figs 14(3a)–(3c) show the attenuation curve $A_{\mathrm{R}}^{\mathrm{E}}(\omega)$ as determined by the three methods. Although the curves obtained by methods 1 and 2 are similar, the curve obtained by method 3 is different. It is difficult to assess the accuracy of these curves.

Figs 14(4a)–(4c) show the corresponding material damping ratio profile. The damping ratio obtained from the SCPT test is also shown, but the results are highly scattered and cannot reliably be used as a reference to assess the quality of the SASW results. Methods 1 and 2 both yield a relatively high material damping ratio of 0.08 at large depths. The damping ratio obtained by method 3 does not exceed a value of 0.05 and decreases with depth.

For each of the different soil profiles, the theoretical wiggle traces $u_z^{\mathrm{T}}(r, t)$, transfer function $\hat{H}_{zz}^{\mathrm{T}}(r, \omega)$ and frequency–wavenumber spectrum $\tilde{H}_{zz}^{\mathrm{T,norm}}(C_r, \omega)$ have been computed with EDT. In these calculations, the density of the soil is assumed to be 1800 kg m$^{-3}$. The results are shown in Fig. 15; they are qualitatively similar to the experimental data shown in Fig. 13.

To facilitate a quantitative assessment of the simulation results, Fig. 16 compares the three theoretical transfer functions $\hat{H}_{zz}^{\mathrm{T}}(r, \omega)$ with the experimental transfer function $\hat{H}_{zz}^{\mathrm{E}}(r, \omega)$ at three source–receiver distances. At 10 m from the source (Fig. 16a), the influence of the material damping ratio $D$ on the transfer function $\hat{H}_{zz}^{\mathrm{T}}(r, \omega)$ is weak, and the three soil profiles yield similar results. For all profiles, the agreement with the experimental data is satisfactory, except in the low-frequency range, where the experimental data are severely affected by seismic noise. At 100 m from the source (Fig. 16c), the influence of the material damping ratio $D$ is stronger, especially in the high-frequency range. As a consequence,

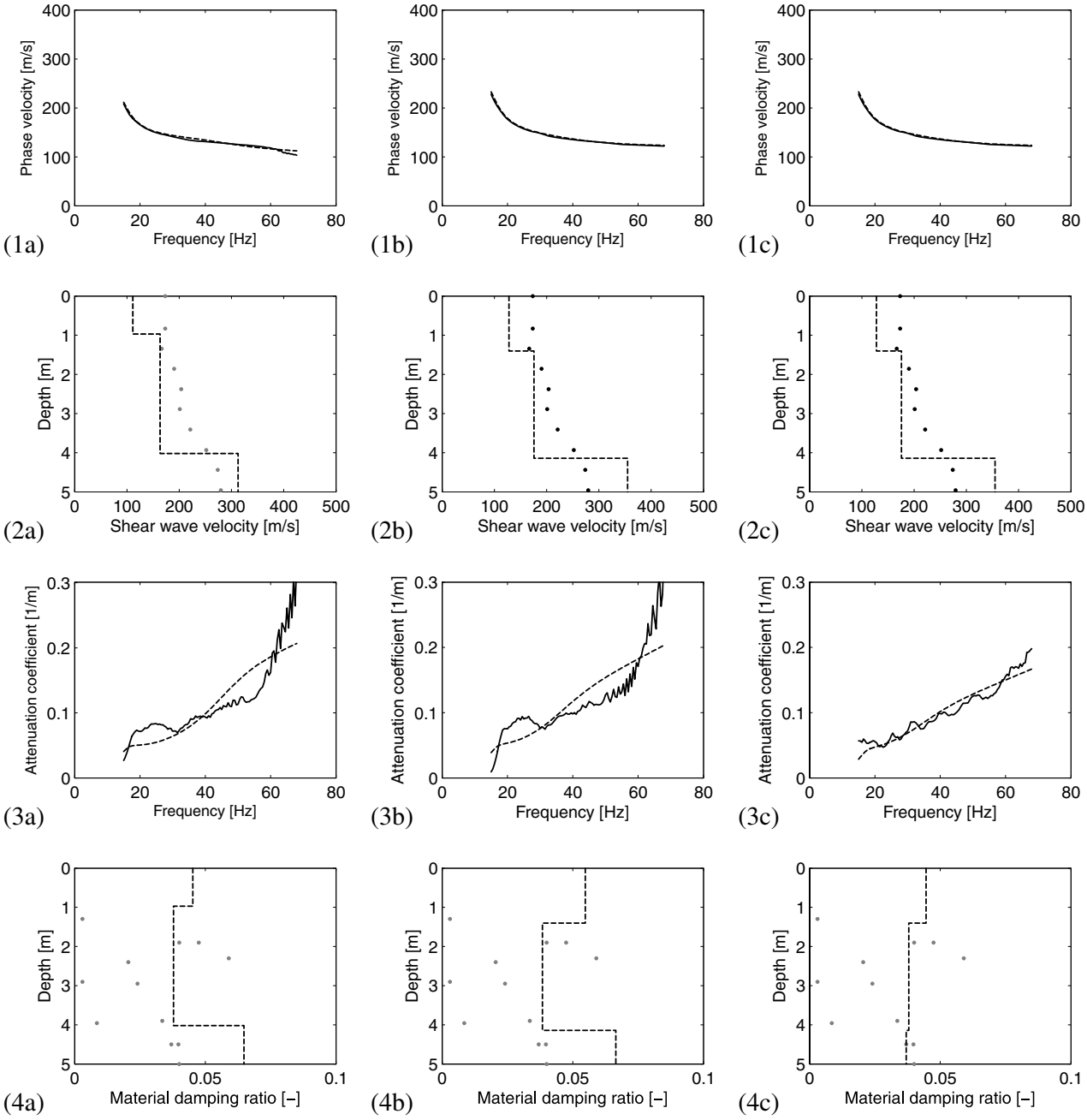


**Figure 14.** (1) Dispersion curve, (2) shear wave velocity, (3) attenuation curve and (4) material damping ratio for the test site in Lincent as determined by (a) method 1, (b) method 2 and (c) method 3. The experimental data (solid black lines) and the theoretical data (dashed black lines) are compared with the SCPT results (grey dots).

differences between the transfer functions $\hat{H}^{\mathrm{T}}_{zz}(r,\omega)$ computed for the three different soil profiles can be observed. The transfer function $\hat{H}^{\mathrm{T}}_{zz}(r,\omega)$ computed for the soil profile determined by method 3 agrees slightly better with the experimental data than the two other transfer functions.

This example demonstrates the adequacy of the new method (method 3) to process real measurement data. The method leads to a soil profile that allows for an accurate simulation of the transfer function $\hat{H}^{\mathrm{E}}_{zz}(r,\omega)$ measured in the SASW test. Moreover, the procedure is straightforward, in the sense that the dispersion and attenuation curves are derived directly from the experimental data, without the need to compute a geometric spreading factor. As a consequence, the new method may proof to be very useful in practice, offering the possibility to obtain robust results on the measurement site and almost in real time.

## 5 CONCLUSION

This paper presents a novel technique to determine the material damping in shallow soil layers by means of an SASW test. Compared to existing methods, where the damping ratio is determined from the spatial decay of the Rayleigh wave, the proposed technique operates in the wavenumber domain. The attenuation curve is

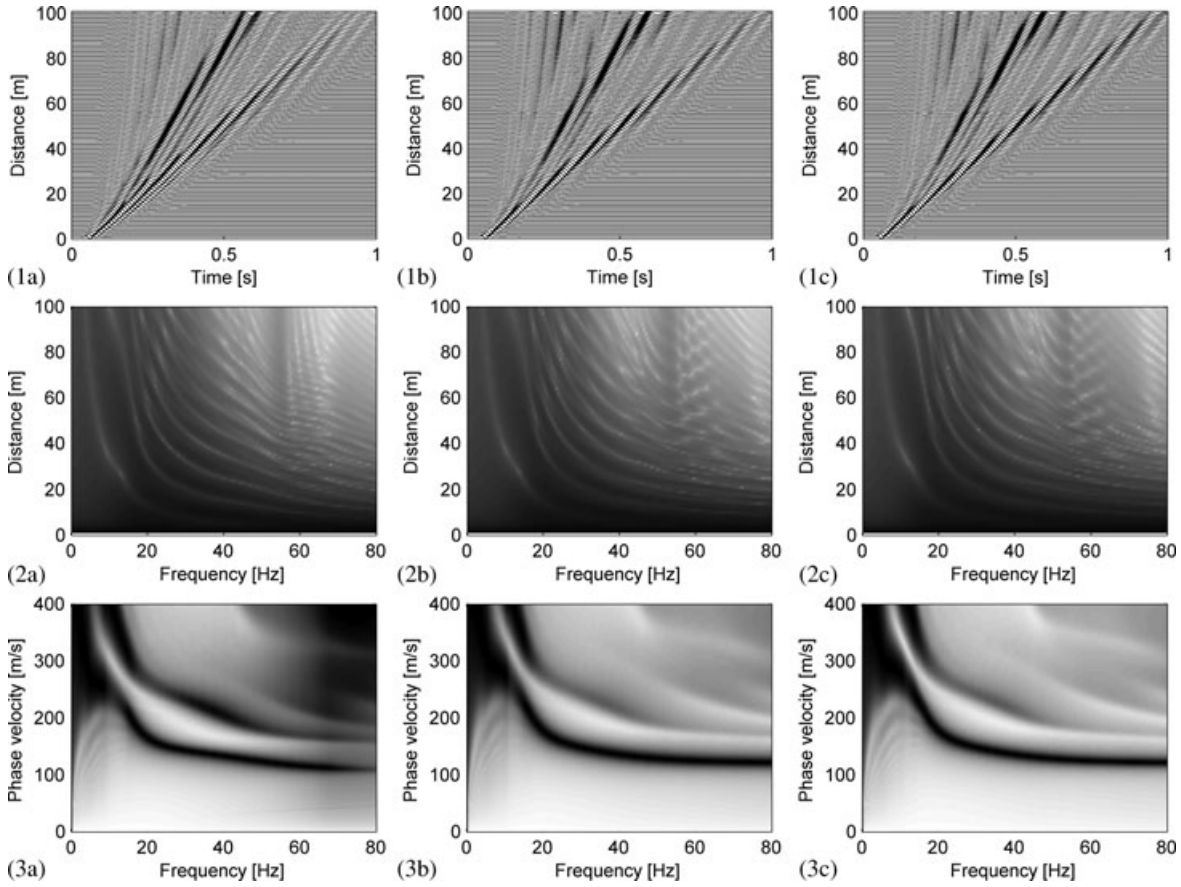


**Figure 15.** (1) Wiggle traces $u_z^{\mathrm{T}}(r, t)$, (2) transfer function $\hat{H}_{zz}^{\mathrm{T}}(r, \omega)$ and (3) frequency–wavenumber spectrum $\tilde{H}_{zz}^{\mathrm{T,norm}}(C_r, \omega)$ for the test site in Lincent, computed for the soil profile obtained with (a) method 1, (b) method 2 and (c) method 3.

derived from the width of the peaks in the frequency–wavenumber spectrum, using the half-power bandwidth method.

Three benchmark problems are considered to compare the new method with two existing methods: a regular soil profile, consisting of a soft layer on a stiffer half-space; an irregular soil profile, with a soft layer trapped between two stiffer layers and a profile where the soil properties vary smoothly with depth. For the regular soil profile, both the existing methods and the new method lead to an adequate estimate of the material damping ratio in the soil. For the irregular soil profile, the new method yields better results than the existing methods. This is due to the contribution of higher modes to the wavefield in the soil: the existing methods are based on the assumption that the wavefield is due to a single surface wave. In the new method, the occurrence of higher modes has no influence on the results, as these modes occur as separate peaks in the frequency–wavenumber spectrum (except at the osculation points). For the smoothly varying soil profile, the new method also yields better results. This is explained by the fact that the existing methods rely on the knowledge of the geometric damping. The geometric damping depends on the shear wave velocity of the soil. Because the shear wave velocity varies smoothly with depth, it is not known exactly, and it is approximated by means of a layered soil profile. As a consequence, the estimation of the geometric damping is also inexact, and the attenuation curve is biased. In the new method, the calculation of the geometric damping is not required due to the use of the appropriate wavenumber transformation: a Hankel transformation is used, so that the cylindrical symmetry of the wave field is properly accounted for and a decomposition of the wavefield in plane waves is obtained.

The existing methods as well as the new method are also applied to experimental data collected from a test site in Belgium. The results are compared with SCPT data. A regular soil profile is obtained, and all three methods lead to a soil profile that allows for an accurate simulation of the wavefield recorded in the SASW test. This application demonstrates the adequacy of the new method to process real measurement data. The new method is expected to be very useful in practice, as the procedure is straightforward and computationally inexpensive. It should, however, be noted that the method involves a number of parameters that must be chosen with care: the strength of the exponential window, the level at which the width of the peak in the frequency–wavenumber spectrum is determined, and the threshold frequency for the attenuation curve. It is suggested to perform a parametric study to determine the most appropriate values for these parameters.

## ACKNOWLEDGMENTS

The results presented in this paper have been obtained within the frame of the project FWO G.0595.06 '*in situ* determination of material damping in the soil at small deformation ratios', funded by the Research Foundation—Flanders and the project OT/05/41 'A generic methodology for inverse modeling of dynamic problems in civil and environmental engineering', funded by the Research

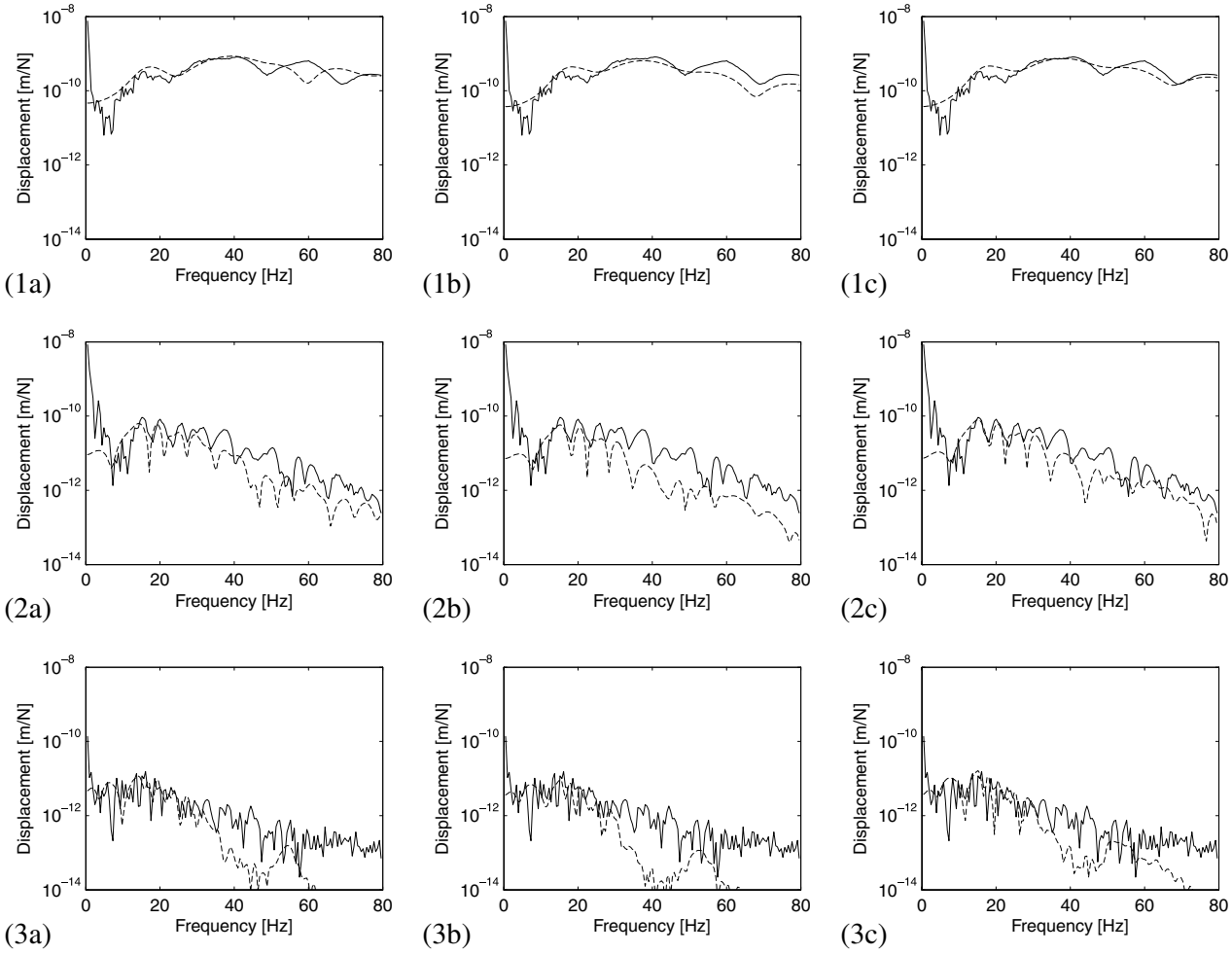


**Figure 16.** Experimental transfer function $\hat{H}_{zz}^{\mathrm{E}}(r, \omega)$ (solid line) and theoretical transfer function $\hat{H}_{zz}^{\mathrm{T}}(r, \omega)$ for the test site in Lincent at (1) 10 m, (2) 50 m and (3) 100 m from the source. The theoretical data correspond to the soil profile obtained with (a) method 1, (b) method 2 and (c) method 3.

Council of K.U. Leuven. The second author is a postdoctoral fellow of the Research Foundation—Flanders.

## REFERENCES

Al-Hunaidi, M., 1994. Analysis of dispersed multi-mode signals of the SASW method using the multiple filter/crosscorrelation technique, *Soil Dyn. Earthq. Eng.,* **13,** 13–24.

Chopra, A., 2007. *Dynamics of Structures*, 3rd edn. Pearson Prentice-Hall, Upper Saddle River, NJ.

Cuellar, V. & Valerio, J., 1997. Use of the SASW method to evaluate soil improvement techniques, in *Proceedings of the 14th international Conference Soil Mechanics and Foundation Engineering*, pp. 461–464.

Ewins, D., 1984. *Modal Testing: Theory and Practice*, Research Studies Press Ltd., Letchworth, UK.

Fladung, W. & Rost, R., 1997. Application and correction of the exponential window for frequency response functions, *Mech. Syst. Signal Process.,* **11**(1), 23–36.

Forbriger, T., 2003a. Inversion of shallow-seismic wavefields: I. Wavefield transformation, *Geophys. J. Int.,* **153**(3), 719–734.

Forbriger, T., 2003b. Inversion of shallow-seismic wavefields: II. Inferring subsurface properties from wavefield transforms, *Geophys. J. Int.,* **153**(3), 735–752.

Foti, S., 2004. Using transfer function for estimating dissipative properties of soils from surface-wave data, *Near Surf. Geophys.,* **2,** 231–240.

Frazer, L. & Gettrust, J., 1984. On a generalization of Filon's method and the computation of the oscillatory integrals of seismology, *Geophys. J. R. astr. Soc.,* **76,** 461–481.

Gucunski, N., 1994. Effects of multiple modes on Rayleigh wave dispersion characteristics, *J. Geotech. Eng., Proc. ASCE,* **120**(1), 466–470.

Guzina, B. & Madyarov, A., 2005. On the spectral analysis of Love waves, *Bull. seism. Soc. Am.,* **95**(3), 1150–1169.

Karl, L., 2005. Dynamic soil properties out of SCPT and bender element tests with emphasis on material damping, *PhD thesis*, Universiteit Gent, Ghent.

Karl, L., Haegeman, W. & Degrande, G., 2006. Determination of the material damping ratio and the shear wave velocity with the Seismic Cone Penetration Test, *Soil Dyn. Earthq. Eng.,* **26**(12), 1111–1126.

Karl, L., Haegeman, W., Degrande, G. & Dooms, D., 2008. Determination of the material damping ratio with the bender element test, *J. Geotech. Geoenviron. Eng., Proc. ASCE,* **134**(12), 1743–1756.

Kausel, E., 2006. *Fundamental Solutions in Elastodynamics: A Compendium*, Cambridge University Press, New York.

Kausel, E. & Roësset, J., 1981. Stiffness matrices for layered soils, *Bull. seism. Soc. Am.,* **71**(6), 1743–1761.

Kavazanjian, E., Snow, M., Poran, C. & Satoh, T., 1994. Non-intrusive Rayleigh wave investigations at solid waste landfills, in *Proceedings of the First International Congress on Environmental Geotechnics*, pp. 707–712, Edmonton.

Lai, C., 1998. Simultaneous inversion of Rayleigh phase velocity and attenuation for near-surface site characterization, *PhD thesis*, Georgia Institute of Technology, Atlanta, GA.

Lai, C., Rix, G., Foti, S. & Roma, V., 2002. Simultaneous measurement and inversion of surface wave dispersion and attenuation curves, *Soil Dyn. Earthq. Eng.,* **22**(9–12), 923–930.

Lombaert, G., Degrande, G., Kogut, J. & François, S., 2006. The experimental validation of a numerical model for the prediction of railway induced vibrations, *J. Sound Vib.,* **297**(3–5), 512–535.

Masoumi, H., Degrande, G. & Lombaert, G., 2007. Prediction of free field vibrations due to pile driving using a dynamic soil-structure interaction formulation, *Soil Dyn. Earthq. Eng.,* **27**(2), 126–143.

McMechan, G. & Yedlin, M., 1981. Analysis of dispersive waves by wave field transformation, *Geophysics,* **46**(6), 869–874.

Nazarian, S. & Desai, M., 1993. Automated surface wave method: field testing, *J. Geotech. Eng., Proc. ASCE,* **119**(7), 1094–1111.

Nazarian, S. & Stokoe, K., II, 1984. Nondestructive testing of pavements using surface waves, *Transport. Res. Record,* **993,** 67–79.

Nazarian, S., Stokoe, K., II & Hudson, W., 1983. Use of spectral analysis of surface waves method for determination of moduli and thicknesses of pavement systems, *Transport. Res. Record,* **930,** 38–45.

Nelder, J. & Mead, R., 1965. A simplex method for function minimization, *Comput. J.,* **7**(4), 308–313.

Pyl, L., Degrande, G., Lombaert, G. & Haegeman, W., 2004. Validation of a source-receiver model for road traffic induced vibrations in buildings. I: Source model, *ASCE J. Eng. Mech.,* **130**(12), 1377–1393.

Rix, G., Lai, C. & Spang, A., Jr, 2000. In situ measurement of damping ratio using surface waves, *J. Geotech. Geoenviron. Eng., Proc. ASCE,* **126**(5), 472–480.

Schevenels, M., Badsar, S. & Degrande, G., 2008a. Application of the SASW method for the determination of stiffness and damping parameters of soils, *International Seminar on Interaction Soil-Railway-Track for High Speed Railways. Geotechnical aspects.* LNEC, Lisbon, Portugal.

Schevenels, M., Lombaert, G., Degrande, G. & François, S., 2008b. A probabilistic assessment of resolution in the SASW test and its impact on the prediction of ground vibrations, *Geophys. J. Int.,* **172**(1), 262–275.

Schevenels, M., François, S. & Degrande, G., 2009. EDT: An ElastoDynamics Toolbox for MATLAB, *Comput. Geosci.,* **35**(8), 1752–1754.